## EDGE ARTICLE

# A design strategy for single-molecule magnet materials with fullerene confinement-induced unpaired f-electrons†

Xiao-Kun Zhao, [ab] Jing Zhao, [a] Shi-Ru Wei, [b] Yun-Ze Qiu, [b] Yang He, [b] Han-Shi Hu [*b] and Jun Li [*abc]

Endohedral metallofullerenes (EMFs) are promising platforms for single-molecule magnets (SMMs) due to their internal cavities, which enable effective coupling of magnetically anisotropic metal ions through direct covalent bonding. However, the practical application of EMF-SMMs remains challenging, particularly in the robust assembly of the cage structures. In this study, we propose a strategy for designing two-dimensional (2D) diactinide EMF-SMM materials ($M_2@C_{60}$-2D, M = U, Th) by doping thorium and uranium into a 2D quasi-hexagonal-phase fullerene ($qHPC_{60}$) monolayer. *Ab initio* molecular dynamics (AIMD) simulations and density functional theory (DFT) calculations confirm the thermal and thermodynamic stability of these materials, suggesting their synthetic feasibility. Further investigations show that fullerene confinement tends to eliminate the traditional Lewis-type electron-pair bonds in neutral $M_2$ dimers and induces multiple single-electron M–M bonding in $M_2@C_{60}$, thus facilitating the enhanced magnetic properties of 2D EMF monolayers. These findings provide valuable insights for designing space-confined metal diatomic systems for magnetic applications.

## Introduction

Single-molecule magnets (SMMs) have attracted significant research interest since the discovery of {Mn₁₂} clusters, owing to their ability to store and process quantum information at the molecular level.[1–3] By utilizing fullerene cages with confined internal nanospace, endohedral metallofullerenes (EMFs) have emerged as promising SMM candidates.[4–7] Dimetallofullerenes (di-EMFs), in particular, exhibit high SMM blocking temperatures and large magnetic anisotropy barriers, making them suitable for applications in quantum information processing and information storage.[8–11]

In di-EMFs of $C_{60}$, direct single-electron metal–metal (M–M) bonds can be formed, which enable strong magnetic coupling between the two metal ions.[12,13] Recently, Long *et al.* reported record SMMs in mixed-valence dilanthanide complexes $(Cp^{iPr5})_2Ln_2I_3$ (Ln = Gd, Tb, Dy, Ho), featuring a single-electron Ln–Ln (d–d)σ bond.[14,15] These findings demonstrated that coupling two magnetic metal ions *via* direct bonding is an

effective strategy for designing high-performance SMMs.[16,17] However, while the 4f orbitals in lanthanides are radially too contracted to form effective chemical bonds, leading to extremely weak direct 4f–4f coupling, the more radially extended and chemically accessible 5f orbitals in actinides make actinide-based EMFs intriguing for exploring unique bonding motifs to achieve stronger magnetic coupling.[18,19]

In 2007, Wu *et al.* proposed six-fold ferromagnetic U–U bonding inside a $U_2@C_{60}$ cage.[20] Gagliardi and colleagues later suggested that these U–U bonds might be artifacts of confinement within the small $C_{60}$ cavity.[21] Similarly, the Straka group described the ferromagnetic U–U bonds in $U_2@C_{80}$ as "unwilling bonding".[22] These theoretical insights spurred experimental investigations into diactinide EMFs. In 2018, Zhang *et al.* provided the first experimental evidence for actinide–actinide bonding in the diuranium endofullerene $U_2@C_{80}$.[19] Shortly thereafter, dithorium endofullerene $Th_2@C_{80}$ was also prepared.[23] Notably, M–M bonding in diactinide EMFs is significantly influenced by the size of the carbon cages, resulting in unpaired single-electron M–M bonds in the $C_{60}$ cage, which further enhance the magnetism of the diactinide EMFs.[24]

The cage assembly of SMMs is crucial for their practical application in information storage. Current approaches include attaching SMMs to conducting surfaces to form 2D molecular assemblies[25–27] and incorporating SMMs into metal–organic frameworks (MOFs) to create 3D molecular structures.[28–30] Recently, the successful synthesis of a two-dimensional quasi-

*aDepartment of Chemistry, Guangdong Provincial Key Laboratory of Catalytic Chemistry, Southern University of Science and Technology, Shenzhen 518055, China*

*bDepartment of Chemistry, Engineering Research Center of Advanced Rare-Earth Materials of Ministry of Education, Tsinghua University, Beijing 100084, China. E-mail: hshu@mail.tsinghua.edu.cn; junli@mail.tsinghua.edu.cn*

*cFundamental Science Center of Rare Earths, Ganjiang Innovation Academy, Chinese Academy of Sciences, Ganzhou 341000, China*

† Electronic supplementary information (ESI) available: Computational details. See DOI: https://doi.org/10.1039/d5sc01607j

hexagonal-phase fullerene (2D qHPC$_{60}$) material has demonstrated distinct electronic structures, showing great potential for applications in physical devices and chemical catalysis.[31–34] Given the single-electron M–M bonds in diactinide EMFs, encapsulating two actinide atoms within a 2D qHPC$_{60}$ monolayer provides a promising approach for developing EMF-SMM materials.

In this work, we have performed a theoretical study on a 2D diactinide EMF monolayer with diactinide doped in the 2D qHPC$_{60}$ monolayer. Our theoretical analyses confirm that these 2D EMF monolayers are thermodynamically stable, indicating their feasibility for experimental synthesis under suitable conditions. Quantum-chemical studies with DFT and CASSCF calculations reveal that fullerene confinement induces single-electron M–M bonding in the encapsulated M$_2$ dimer, contributing to the magnetism of the 2D fullerene monolayer. It is found that U$_2$@C$_{60}$-2D exhibits an interfullerene antiferromagnetic (AFM) singlet ground state, attributed to the U$_2$–C$_{60}$···C$_{60}$–U$_2$ super-superexchange interactions along the interfullerene [2 + 2] cycloaddition bonds. In contrast, Th$_2$@C$_{60}$-2D has an interfullerene ferromagnetic (FM) ground state. Our findings present a novel strategy for designing space-confined EMF-SMM materials that could provide insights for designing high-density information storage, quantum computing, and molecular spintronic devices.

## Results and discussion

### Geometric structure of 2D diactinide EMF monolayers: M$_2$@C$_{60}$-2D (M = Th, U)

The experimentally synthesized 2D qHPC$_{60}$ monolayer features each C$_{60}$ molecule surrounded by six neighbouring cages, forming a hexagonal lattice with a space group of *Pmna*. Among these neighbours, four are linked by interfullerene C–C single bonds and two are connected through interfullerene [2 + 2] cycloaddition bonds. The interfullerene bonds reduce the local symmetry of C$_{60}$ from $I_h$ to $C_{2h}$ in the 2D qHPC$_{60}$ monolayer. Therefore, the 20 hexagonal rings of C$_{60}$ can be categorized into six distinct types (positions 1 to 6 in Scheme 1). Both



Scheme 1 The geometric structure of the 2D qHPC$_{60}$ monolayer and its constituent C$_{60}$ unit with local $C_{2h}$ symmetry. The numbers indicate the six distinct types of hexagonal rings found within the $C_{2h}$-symmetric C$_{60}$ unit.

experimental and theoretical studies have revealed that encapsulated diactinide dimers in EMFs tend to be sandwiched between two hexagonal rings.[19–21,23] We initially explored the encapsulation sites of actinide dimers within distorted $C_{2h}$ C$_{60}$ cages by constructing six different diuranium EMF models based on U$_2$@C$_{66}$H$_{20}$. In these models, the U$_2$ dimer was placed at the centroids of six distinct hexagonal rings (positions 1 to 6). Geometry optimizations identified position 1 as the most favourable (Fig. S1†), where the U$_2$ dimer is encapsulated while preserving the $C_{2h}$ symmetry.

We then constructed the 2D diactinide EMF monolayers with M$_2$ dimers located at position 1. The calculated geometric structure shows that both U$_2$@C$_{60}$-2D and Th$_2$@C$_{60}$-2D monolayers share the same structure and symmetry as the 2D qHPC$_{60}$ monolayer (Fig. 1). The lattice and structural parameters are compared to those of the 2D qHPC$_{60}$ monolayer (Table 1). The lattice lengths of the *a*-axis and *b*-axis are 15.90 and 9.24 Å for the U$_2$@C$_{60}$-2D monolayer, and 15.80 and 9.20 Å for the Th$_2$@C$_{60}$-2D monolayer, respectively, showing slight elongation along the *b*-axis and shrinkage along the *a*-axis when compared to the 2D qHPC$_{60}$ monolayer. Furthermore, the bond lengths of interfullerene C–C single bonds and [2 + 2] cycloaddition bonds remain virtually unchanged in both the pristine 2D fullerene monolayer and M$_2$@C$_{60}$-2D. The calculated M–M bond distances are 2.70 Å for U–U and 2.86 Å for Th–Th, which are comparable to the sum of the Pyykkö covalent double-bond radii of 2.68 Å for U=U and of 2.86 Å for Th=Th.[35] Notably, the space-confined Th–Th distance is notably shorter than that reported for thorium systems such as the tri-thorium cluster (3.99 Å)[36] and the dithorium complex (4.01 Å).[37] These relatively short M–M bond lengths in our system indicate strong bonding interactions between two endohedral actinide atoms under the structure confinement of the fullerene cage. In addition, the M–C contacts range from 2.46 to 2.48 Å for U–C bonds and from 2.48 to 2.50 Å for Th–C bonds, suggesting strong bonding interactions between the encapsulated M$_2$ dimers and the adjacent carbon atoms of the C$_{60}$ cages.

### Stability analysis

The phonon spectrum that describes lattice vibration in crystals is relevant to its stability with respect to structural phase transitions or other distortions. Our 2D diactinide EMF monolayers do not show imaginary phonon modes despite the numerical noise, indicating dynamic stability of these monolayers (Fig. S2 and S3†). To investigate the thermal stability, we conducted temperature-accelerated AIMD simulations at various high temperatures, each for 10 ps, to enhance the atomic mobility and explore a larger configurational space in a shorter simulation time. The temperatures used are $T$ = 1400, 1800, 2200, and 2600 K for U$_2$@C$_{60}$-2D and $T$ = 600, 1000, 1400, and 1800 K for Th$_2$@C$_{60}$-2D. The AIMD simulations reveal that U$_2$@C$_{60}$-2D exhibits greater thermal stability. The hexagonal framework of U$_2$@C$_{60}$-2D remains intact up to 2200 K (Fig. S4†), whereas Th$_2$@C$_{60}$-2D is stable only up to 1400 K (Fig. S5†). The 2D fullerene framework breaks down into single C$_{60}$ molecules at 2600 K for U$_2$@C$_{60}$-2D and at 1800 K for Th$_2$@C$_{60}$-2D. These
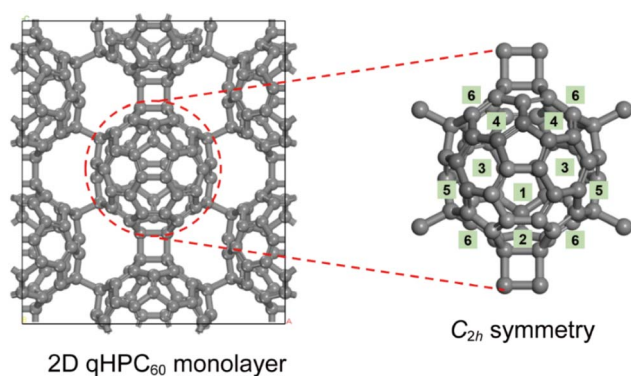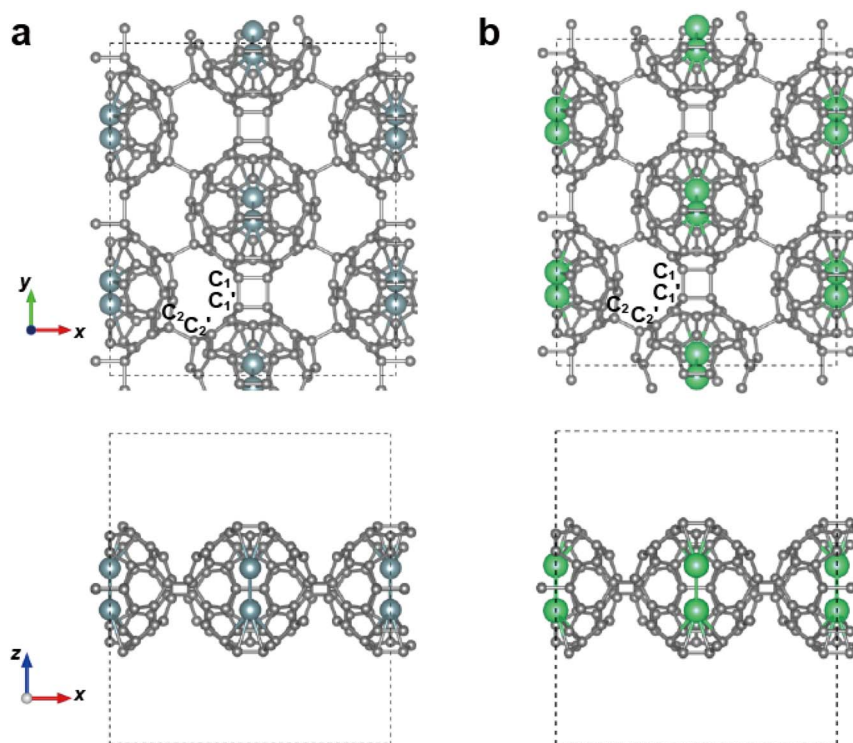
**Fig. 1** Top view and side view of the 2D diactinide EMF monolayer. (a) $U_2@C_{60}$-2D monolayer, and (b) $Th_2@C_{60}$-2D monolayer. $C_1$ and $C_1'$ represent the C atoms of the interfullerene [2 + 2] cycloaddition bond. $C_2$ and $C_2'$ represent the C atoms of the interfullerene C–C single bond.

**Table 1** Comparison of lattice and geometric structure parameters between the 2D qHPC60 monolayer and the 2D diactinide EMF monolayers

| | 2D qHPC$_{60}$ | $U_2@C_{60}$-2D | $Th_2@C_{60}$-2D |
|---|---|---|---|
| **Lattice parameters** | | | |
| $a$ (Å) | 15.92 | 15.90 | 15.80 |
| $b$ (Å) | 9.16 | 9.24 | 9.20 |
| **Interfullerene bond** | | | |
| C–C single bonds (Å) | 1.61 | 1.59 | 1.60 |
| [2 + 2] cycloaddition bonds (Å) | 1.61 | 1.62 | 1.61 |
| M–M bond (Å) | | 2.70 | 2.86 |
| M–C bond (Å) | | 2.46–2.48 | 2.48–2.50 |

results indicate that encapsulating the $U_2$ dimer enhances the stability of the 2D fullerene monolayer, while $Th_2$ dimer doping has little influence on stability.[33]

The stability of these fullerene monolayers was further elucidated through crystal orbital Hamilton population (COHP) analysis, which reconstructs orbital-resolved wavefunctions *via* projecting delocalized plane-wave basis functions into localized atomic-like basis sets.[38] This analysis aims at describing the interaction between two orbitals centred at neighbouring atoms by considering the product of their corresponding Hamiltonian matrix element and the density-of-states matrix, thus measuring the bonding contribution and bonding strength between neighbouring atoms upon integrating the COHP below the Fermi level. The integrated projected COHP (IpCOHP) of interfullerene bonds in the 2D qHPC$_{60}$ monolayer is about −7.90 eV (Table S1†). In

contrast, the IpCOHP values of the [2 + 2] cycloaddition bonds and C–C single bonds in $U_2@C_{60}$-2D are up to −8.46 and −8.49 eV, respectively, compared to −7.82 and −8.03 eV in $Th_2@C_{60}$-2D. Consequently, the $U_2@C_{60}$-2D monolayer is more stable than the pristine 2D qHPC$_{60}$ monolayer. Furthermore, to quantitatively evaluate changes in the 2D fullerene framework during AIMD simulations, we examined the bond length variations of interfullerene bonds $C_1 - C_1'$ (four-membered ring bond) and $C_2 - C_2'$ (single bond). The bond lengths of $C_1 - C_1'$ and $C_2 - C_2'$ in $U_2@C_{60}$-2D fluctuate around the equilibrium bond length in simulations at temperatures below 2200 K (Fig. S8†). However, at 2600 K, these bond lengths experience significant changes after 4 ps of simulation, indicating the collapse of the 2D hexagonal structure. Similarly, the $Th_2@C_{60}$-2D monolayer undergoes fission after 5 ps of simulations at 1800 K (Fig. S9†). Additionally, the U–U and Th–Th bonds oscillate around their equilibrium bond length even after the 2D EMF monolayers break down into individual EMF cages.

To verify the thermodynamic feasibility of synthesizing these 2D diactinide EMF monolayers, we computed the Gibbs free energies from the reactants (2D qHPC$_{60}$ monolayer and bulk uranium or thorium metal). The proposed reaction is shown in eqn (1):

$$2M \text{ (bulk)} + 2D \text{ qHPC}_{60} \rightarrow M_2@C_{60}\text{-2D} \quad (1)$$
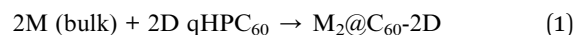
The Gibbs free energy of the reactants, corrected for entropy and zero-point energies, is provided in Table S2.† The Gibbs free energy ($\Delta G_{300 \text{ K}}$) at 300 K was calculated using the formula

$\Delta G_{300\ \text{K}} = G(\text{M}_2@\text{C}_{60}\text{-2D})_{300\ \text{K}} - 2G(\text{M}_{\text{bulk}})_{300\ \text{K}} - G(\text{2D qHPC}_{60})_{300\ \text{K}}$. The calculated $\Delta G_{300\ \text{K}}$ is negative ($-3.02$ kcal mol$^{-1}$) for the formation of the U$_2$@C$_{60}$-2D monolayer, but positive ($+14.8$ kcal mol$^{-1}$) for the Th$_2$@C$_{60}$-2D monolayer, indicating the experimental feasibility of the U$_2$@C$_{60}$-2D monolayer under ambient conditions. Despite the endergonic feature, the possibility of experimental preparation of the Th$_2$@C$_{60}$-2D monolayer cannot be excluded because it remains metastable.

## Single-electron actinide–actinide bonds in 2D fullerene

DFT calculations reveal that the actinides of the encapsulated M$_2$ dimers exhibit a ferromagnetic state (Table S3†), with calculated magnetic moments 2.75 $\mu_{\text{B}}$ for uranium (U) and 0.68 $\mu_{\text{B}}$ for thorium (Th) atoms. We used Bader charge analysis to assist the determination of the oxidation states of encapsulated actinides by comparing with reported EMFs, including U$_2$@C$_{80}$,[19] U$_2$C$_2$@C$_{80}$,[39] Th$_2$@C$_{80}$,[23] and ThC$_2$@C$_{82}$.[40] Previous experimental and quantum-chemical calculation results
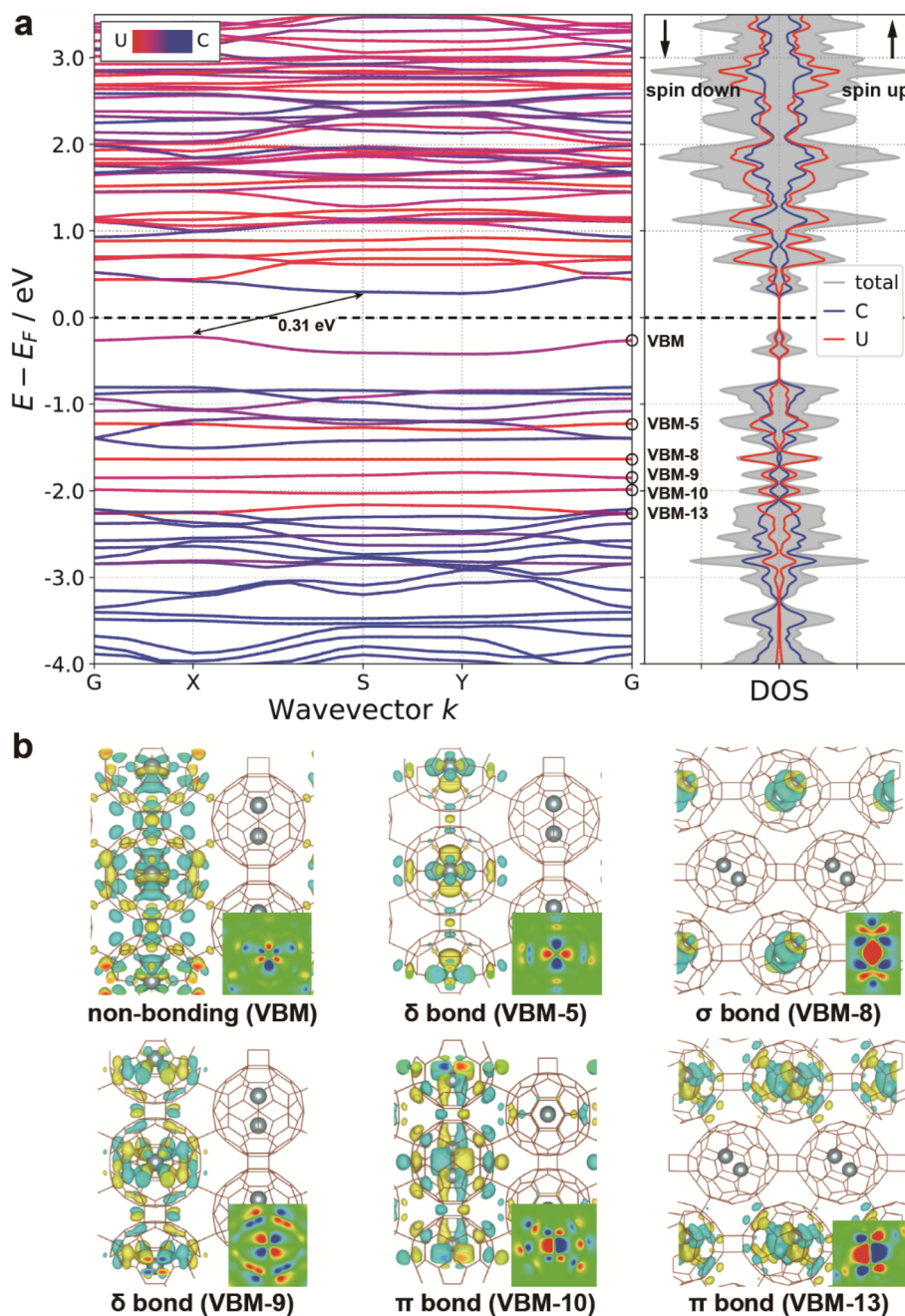


**Fig. 2** (a) Band structure and projected density of states (pDOS) at the HSE06 level for the U$_2$@C$_{60}$-2D monolayer. The high-symmetry points in the first Brillouin zone of reciprocal space are denoted as G (0, 0, 0), X (0.5, 0, 0), S (0.5, 0.5, 0) and Y (0, 0.5, 0). The red curves represent contributions from uranium (U), while the blue curves indicate contributions from carbon (C) atoms. (b) Spin-up real-space wave functions for the bands at the G point illustrate the bonding patterns of the U$_2$ dimer. Note that only the real space wave functions of a single EMF cage are shown due to the interfullerene AFM state of the U$_2$@C$_{60}$-2D monolayer.

indicate that U has a formal oxidation state of +4 in $U_2C_2@C_{80}$ and +3 in $U_2@C_{80}$. The Bader charges for $U^{4+}$ and $U^{3+}$ in these EMFs are +2.00 and +1.54, respectively (Table S4†). In $U_2@C_{60}$-2D, the Bader charge of U is +1.45, which is close to +1.54 observed for $U^{3+}$ in $U_2@C_{80}$, suggesting a +3 formal oxidation state for encapsulated U atoms. Similarly, the Bader charge for Th in $Th_2@C_{60}$-2D is +1.64, comparable to the +1.68 in $Th_2@C_{80}$, indicating a +3 formal oxidation state for Th atoms. Thus, the valence state of the $M_2@C_{60}$-2D monolayer can be described as a $(M_2)^{6+}@(C_{60}\text{-2D})^{6-}$ assignment.

As depicted in Fig. 2(a), the $U_2@C_{60}$-2D monolayer has an indirect energy gap of 0.31 eV, which is significantly smaller than the 1.6 eV band gap of the 2D $qHPC_{60}$ monolayer. This reduction is attributed to the charge transfer from the $U_2$ dimer to the $C_{60}$ cage. In the band structure, several red flat bands below the Fermi level are ascribed to the f-bonding orbitals of the $U_2$ dimer, as confirmed by the projected density of states (pDOS). The valence band minimum (VBM) results from inter-actions between the $U_2$ dimer and the $C_{60}$ cage, with real-space wavefunctions indicating φ-type non-bonding orbitals of $U_2$ interacting with the $C_{60}$ cage.[41]

The f-bonding orbitals are further revealed by the real-space wavefunctions shown in Fig. 2(b). Specifically, VBM-5 and VBM-9 correspond to U(5f) δ-bonding orbitals, VBM-8 corresponds to U(5f) σ-bonding orbitals, and VBM-10 and VBM-13 correspond to U(5f) π-bonding orbitals. Therefore, there are five single-electron U–U bonds formed within EMF cages. The calculation of the $U_2@C_{68}H_{20}$ molecular model further confirms the five single-electron U–U bonds, consistent with the solids model calculation results (Fig. S10 and S11†). Additionally, the calculated band structure and projected DOS reveal Th–Th bonding in the $Th_2@C_{60}$-2D monolayer. As shown in Fig. S12,† spin-up real-space wavefunctions show two nearly degenerate single-electron Th–Th π bonds in EMF cages. The orbital interaction diagram for the $Th_2@C_{68}H_{20}$ molecular model confirms two degenerate Th–Th π bonds (40 $a_u$ and 50 $b_u$) in the encapsulated $Th_2$ dimer as well (Fig. S13 and S14†).

Natural localized molecular orbitals (NLMOs) from one-electron reduced density matrix analysis provide insight into the nature of actinide–actinide bonding in diactinide EMF cages. Fig. 3 shows five single-electron NLMOs, comprising one σ bond, two π bonds, and two δ bonds, primarily contributed by U(5f) orbitals (with minor 6d character) within the $U_2@C_{68}H_{20}$ cage. In contrast, the $Th_2@C_{68}H_{20}$ cage forms only two π bonds, with Th(5f) and Th(6d) orbitals contributing almost equally. To verify the multiconfigurational character of single-electron actinide–actinide bonds, we performed complete-active-space self-consistent field (CASSCF) calculations. As shown in Fig. S15,† the U–U bonding can be interpreted as $\sigma^1\pi^2\delta^2 f^1$, with an effective bond order (EBO) of 1.90. The Th–Th bonding of the $Th_2@C_{68}H_{20}$ molecule model consists of two single-electron π bonds with an EBO of 0.98 (Fig. S16†). As a result, the CASSCF calculations further confirm the single-electron M–M bonding formed in the 2D EMF monolayers. Additionally, relativistic effects significantly influence heavier elements and their compounds, particularly in the bonding patterns of diatomic molecules.[42] The effect of spin–orbit coupling (SOC) was examined by comparing it with the scalar relativistic (SR) states to understand the nature of the U–U and Th–Th bonding in the diactinide EMFs. As shown in Fig. S17 and S18,† the SOC effect does not significantly alter the U–U and Th–Th bonding scheme compared to the SR results. Therefore, the SR results can accurately describe bonding motifs of U–U and Th–Th.

### The role of fullerene confinement in single-electron bond formation

In addition to the ferromagnetic state of encapsulated $M_2$ dimer observed in individual EMF cages in solids (Table S3†), cluster models also show a preference for high-spin states. Specifically, $U_2@C_{68}H_{20}$ adopts a septet ground state, while $Th_2@C_{68}H_{20}$ favours a triplet ground state (Table S5†), both exhibiting ferromagnetic single-electron bonds within the EMFs. To further investigate the mechanism behind the formation of these single-electron bonds, simplified $U_2@C_{60}$ and $Th_2@C_{60}$ models with $D_{3d}$ symmetry were used.[20,24]

As illustrated in Fig. 4, the neutral $Th_2$ molecule exhibits a quadruple bonding scenario consisting of $(7s\sigma_g)^2(6d\pi_u)^4(6d\sigma_g)^1(6d\delta_g)^1$.[43] However, similar to the case of ligand-destabilized $d_{x^2-y^2}$ antibonding orbitals in the $[Re_2Cl_8]^{2-}$ dianion of Cotton's multiple bonding model,[44] the quadruple bonds in $Th_2$ are disrupted when encapsulated inside the fullerene due to strong Th–fullerene interactions. Furthermore, the hybridization of the 6d and 5f orbitals in $Th^{3+}$ is highly effective because of the small 6d–5f energy gap (Fig. S20†), allowing the 5fπ and 6dπ bonding orbitals to hybridize and form two more stable (f–d)π bonding orbitals (see details in Fig. S21†). However, the encapsulated $Th_2^{6+}$ dimer contains only two electrons, resulting in the formation of two degenerate single-electron Th–Th (f–d)π bonds in the $Th_2@C_{60}$ molecule.

In the case of the $U_2@C_{60}$ molecule, strong U–fullerene interactions eliminate the $(7s\sigma_g)^2$ and $(6d\pi_u)^4$ electron-pair bonds from the valence manifold of neutral $U_2$, leaving only the 5f electrons available for U–U bonding.[45] However, the U(5f)
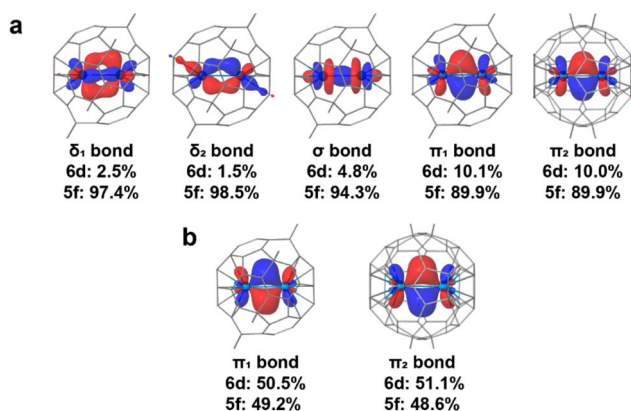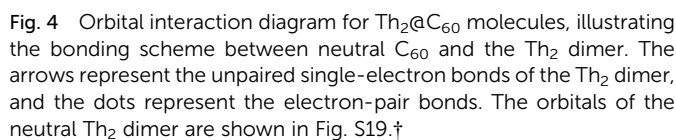


Fig. 3 Natural localized molecular orbitals (NLMOs). (a) Five single-electron NLMOs of the $U_2$ dimer in the $U_2@C_{68}H_{20}$ molecular model, and (b) two single-electron NLMOs of the $Th_2$ dimer in the $Th_2@C_{68}H_{20}$ molecular model. The hydrogen atoms are omitted for clarity. (Isovalue = 0.04 a.u.)

**Fig. 4** Orbital interaction diagram for $Th_2@C_{60}$ molecules, illustrating the bonding scheme between neutral $C_{60}$ and the $Th_2$ dimer. The arrows represent the unpaired single-electron bonds of the $Th_2$ dimer, and the dots represent the electron-pair bonds. The orbitals of the neutral $Th_2$ dimer are shown in Fig. S19.†

orbitals are radially too contracted to form effective Lewis-type electron-pair bonds at the relatively long U–U distance of 2.70 Å. Instead, single-electron bonds are energetically more favourable due to the exchange stabilization, leading to the formation of five single-electron U–U bonds in the $U_2@C_{60}$ molecule (Fig. S22 and S23†).

Additionally, the atomic radial distribution function (RDF) curves in Fig. S24† provide insights into the U–fullerene orbital interactions, revealing a stronger overlap between U(6d) and C(2p) orbitals compared to U(5f) and C(2p) orbitals. Further analysis using principal interacting orbital (PIO) and energy decomposition analysis with the extension of natural orbitals for chemical valence (EDA-NOCV) methods for the encapsulated $U_2$ and $C_{60}$ fragments show that the U(6d) orbitals play a more significant role in U–fullerene bonding interaction than U(5f) orbitals (Fig. S25 and S26†).

The single-electron M–M bonds within $M_2@C_{60}$ represent a balance between M–M bonding and M–fullerene interactions. The confinement effect of the fullerene is evident in the projected DOS of neutral $C_{60}$, $M_2$ and $M_2@C_{60}$ molecules (Fig. S27†). The strong electron-pair bonds in neutral $M_2$ dimers, primarily contributed by 7s and 6d orbitals, are shifted to unoccupied states within $M_2@C_{60}$ due to the $M_2$–fullerene orbital interaction with space-confinement. This shift results in the formation of single-electron M–M bonds, which are responsible for introducing magnetism into 2D diactinide EMF monolayers.

The COHP analysis provides valuable insights into the relationships between magnetic states and the bonding characteristics of encapsulated $M_2$ dimers from the perspective of chemical bonding in solids.[38] As shown in Fig. S28,† the non-spin-polarized COHP curves indicate that the Fermi levels in antiferromagnetic $M_2$ dimers cross the bonding regions of the

M–M COHP curves, leaving many bonding orbitals unoccupied. In contrast, for ferromagnetic $M_2$ dimers, the spin-polarized COHP curves show that the spin-up states occupy lower energy levels, while the spin-down states shift upward. As a result, most of the spin-up bonding states are positioned below the Fermi levels, resulting in strengthened M–M bonding (0.24 eV for U–U and 0.44 eV for Th–Th). Moreover, the single-electron M–M bonding strength, calculated as IpCOHP(spin up) − IpCOHP(spin down), reveals bonding strengths of −3.28 eV for U–U and −2.31 eV for Th–Th.

### Magnetism in 2D diactinide EMF monolayers

As the fullerene confinement can significantly affect the bonding between the diactinide metals, the magnetic properties of the solid are dictated by the competition of the fullerene–metal and metal–metal interactions. To further investigate the magnetic properties in these 2D diactinide EMF monolayers, we constructed a supercell model with three different interfullerene magnetic states: ferromagnetic (FM), antiferromagnetic (AFM), and antiferromagnetic/ferromagnetic (AF/FM) states (Fig. S29†). In these magnetic states, the electrons of $M_2$ dimers are ferromagnetic and are represented by a single red arrow, indicating the orientation of the magnetic moment of the unpaired electrons in the encapsulated $M_2$ dimers (displayed in Fig. 5). DFT calculation results, as shown in Table S6,† reveal that the $U_2@C_{60}$-2D monolayer has an interfullerene AFM singlet ground state, which is more stable than the ferromagnetic (FM) state by 36.4 meV per $U_2$ dimer. In contrast, the ground state of the $Th_2@C_{60}$-2D monolayer is the interfullerene FM state.

$$H = -J \sum_{i<j} \vec{S}_i \cdot \vec{S}_j + H_0 \qquad (2)$$

In addition, the Heisenberg model (see eqn (2)) with FM, AFM, and AF/FM states was applied to calculate the exchange coupling constants along the interfullerene [2 + 2] cycloaddition bonds ($J_1$, represented by the blue solid lines) in Fig. 5, and along interfullerene C–C single bonds ($J_2$, represented by the green dashed lines). In eqn (2), $J$ is the exchange coupling constant, $H_0$ is the nonmagnetic Hamiltonian, and $\vec{S}_i$ and $\vec{S}_j$ are the spin momentum at sites $i$ and $j$, respectively. The exchange coupling constant $J_1$ is calculated to be −16.1 cm$^{-1}$ and $J_2 = -0.3$ cm$^{-1}$, leading to an interfullerene AFM ground state within the $U_2@C_{60}$-2D monolayer.[46] Since each $U_2$ dimer has six unpaired electrons, a 1D Heisenberg antiferromagnetic chain with $S = 3$ on encapsulated $U_2$ dimers forms in the $U_2@C_{60}$-2D monolayer due to the relatively small $J_2$ exchange coupling ($J_2 \ll J_1$). In the $Th_2@C_{60}$-2D monolayer, the calculated exchange coupling constants $J_1$ (6.4 cm$^{-1}$) and $J_2$ (5.4 cm$^{-1}$) are comparable, leading to an interfullerene ferromagnetic ground state.

The interfullerene AFM ground state of the $U_2@C_{60}$-2D monolayer is further evaluated using EDA-NOCV for cluster models of the $(C_{66}H_{16})_2$, $(Th_2@C_{66}H_{16})_2$, and $(U_2@C_{66}H_{16})_2$ dimers, where the $C_{60}$ cages are connected by [2 + 2] cycloaddition bonds. The orbital interactions constitute approximately
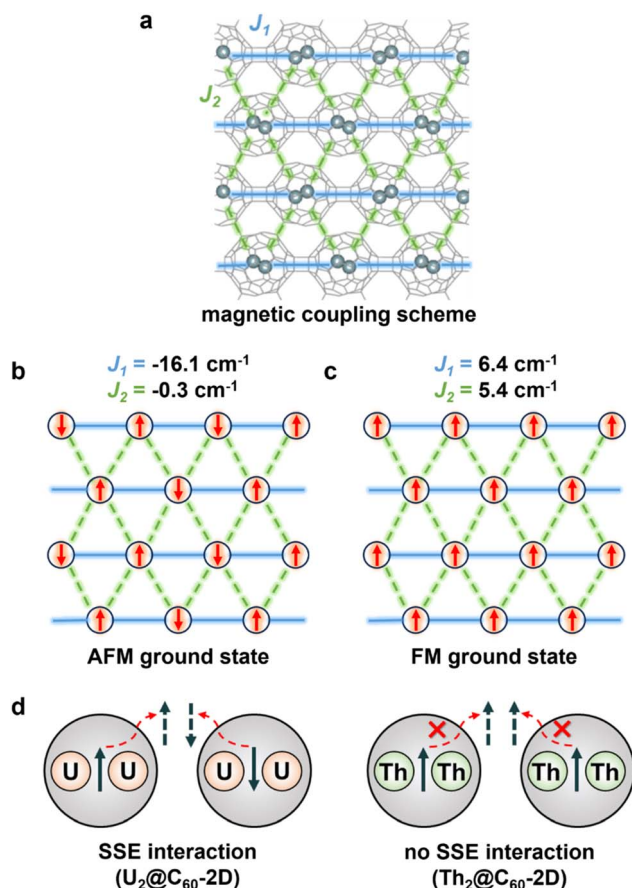
**Fig. 5** (a) Magnetic coupling scheme of 2D diactinide EMF monolayers. Schematic presentation of the (b) AFM ground state of $U_2@C_{60}$-2D and (c) FM ground state of the $Th_2@C_{60}$-2D monolayer. (d) Schematic representation of super-superexchange (SSE) interactions in $U_2@C_{60}$-2D and $Th_2@C_{60}$-2D monolayers. The magnetic coupling along the interfullerene [2 + 2] cycloaddition bonds and C–C single bonds is indicated by the blue solid lines ($J_1$) and green dashed lines ($J_2$), respectively.

60% of the total interactions between two EMF fragments in molecular dimers, indicating a significant covalent bonding character among these 2D EMF monolayers (see Tables S7–S9† for details). The NOCV deformation densities between two EMF fragments are summarized in Fig. S30.† The third deformation orbital of the $(U_2@C_{66}H_{16})_2$ dimer, highlighted in the red box, reveals that the 5f orbitals of the $U_2$ dimer contribute about 5.0% to the orbital interactions between two $U_2@C_{66}H_{16}$ fragments. In contrast, the EDA-NOCV analysis of the $(Th_2@C_{66}H_{16})_2$ dimer is similar to the $(C_{66}H_{16})_2$ dimer, showing no f-orbital involvement.

The f-orbital involved interfullerene interaction in the $(U_2@C_{66}H_{16})_2$ dimer suggests a possible pathway for the super-superexchange (SSE) interactions[47–49] among encapsulated $U_2$ dimers in different EMF cages, which results in the AFM ground state in the $U_2@C_{60}$-2D monolayer. As illustrated in Fig. 5(d), the unpaired f-orbital electrons (solid arrows) of the $U_2$ dimer can hop to the unoccupied orbitals of the $C_{60}$ cage (dashed arrows), and then interact with electrons of opposite spin in the adjacent $C_{60}$ cage, thereby stabilizing the $U_2@C_{60}$-2D monolayer. These $U_2$–$C_{60}\cdots C_{60}$–$U_2$ SSE interactions help explain the AFM ground state of the $U_2@C_{60}$-2D monolayer. In contrast, the $Th_2@C_{60}$-2D monolayer lacks f-orbital mediated interfullerene interactions, resulting in a ferromagnetic ground state.

## Conclusions

In summary, we present a strategy for designing EMF-SMM materials by doping diactinide into a 2D qHPC$_{60}$ monolayer. Through DFT calculations and AIMD simulations, we confirm the dynamic, thermal, and thermodynamic stability of these monolayers, demonstrating their feasibility in experimental preparation. The oxidation states of Th and U in the $M_2@C_{60}$-2D monolayer are assigned as +3, which corresponds to a $(M_2)^{6+}@(C_{60}$-2D$)^{6-}$ charge state. This relative low oxidation states of $Th^{+3}$ and $U^{+3}$ are attributed to the low electronegativity of the $C_{60}$ cage, which disfavours high oxidation states of actinides. Theoretical investigations, including DFT and multi-configurational *ab initio* CASSCF calculations on molecular models, reveal that fullerene confinement induces single-electron M–M bonds in diactinide EMFs, enhancing the magnetic properties of these 2D monolayers. Further supercell model calculations using periodic DFT reveal that the $U_2@C_{60}$-2D monolayer adopts an interfullerene AFM singlet ground state, driven by strong exchange coupling *via* $U_2$–$C_{60}\cdots C_{60}$–$U_2$ super-superexchange interactions along the interfullerene [2 + 2] cycloaddition bonds. In contrast, the $Th_2@C_{60}$-2D monolayer displays an interfullerene FM ground state. This study expands our understanding of fullerene confinement and its role in promoting unique single-electron M–M bonding and magnetism, offering a novel strategy for designing EMF-SMM materials.

## Data availability

The data supporting the findings of this study are available from the corresponding author upon reasonable request.

## Author contributions

J. L. and H.-S. H. conceived and directed the research. X.-K. Z. performed all the calculations. X.-K. Z., J. Z., and S.-R. W. designed the study and analysed the data. Y.-Z. Q. assisted with the CASSCF calculations. Y. H. contributed to the discussion of magnetic calculations. X.-K. Z., H.-S. H. and J. L. co-wrote the paper. All the authors discussed the results and provided comments on the manuscript.

## Conflicts of interest

There are no conflicts to declare.

## Acknowledgements

# References

1 R. Sessoli, D. Gatteschi, A. Caneschi and M. A. Novak, *Nature*, 1993, **365**, 141–143.

2 M. N. Leuenberger and D. Loss, *Nature*, 2001, **410**, 789–793.

3 M. Shiddiq, D. Komijani, Y. Duan, A. Gaita-Ariño, E. Coronado and S. Hill, *Nature*, 2016, **531**, 348–351.

4 Z. Hu, Y. Wang, A. Ullah, G. M. Gutiérrez-Finol, A. Bedoya-Pinto, P. Gargiani, D. Shi, S. Yang, Z. Shi, A. Gaita-Ariño and E. Coronado, *Chem*, 2023, **9**, 3613–3622.

5 F. Liu, D. S. Krylov, L. Spree, S. M. Avdoshenko, N. A. Samoylova, M. Rosenkranz, A. Kostanyan, T. Greber, A. U. B. Wolter, B. Buchner and A. A. Popov, *Nat. Commun.*, 2017, **8**, 16098.

6 F. Liu, L. Spree, D. S. Krylov, G. Velkos, S. M. Avdoshenko and A. A. Popov, *Acc. Chem. Res.*, 2019, **52**, 2981–2993.

7 R. Westerström, J. Dreiser, C. Piamonteze, M. Muntwiler, S. Weyeneth, H. Brune, S. Rusponi, F. Nolting, A. Popov, S. Yang, L. Dunsch and T. Greber, *J. Am. Chem. Soc.*, 2012, **134**, 9840–9843.

8 W. Fu, J. Zhang, T. Fuhrer, H. Champion, K. Furukawa, T. Kato, J. E. Mahaney, B. G. Burke, K. A. Williams, K. Walker, C. Dixon, J. Ge, C. Shu, K. Harich and H. C. Dorn, *J. Am. Chem. Soc.*, 2011, **133**, 9741–9750.

9 G. Velkos, D. S. Krylov, K. Kirkpatrick, X. Liu, L. Spree, A. U. B. Wolter, B. Büchner, H. C. Dorn and A. A. Popov, *Chem. Commun.*, 2018, **54**, 2902–2905.

10 Z. Hu, B.-W. Dong, Z. Liu, J.-J. Liu, J. Su, C. Yu, J. Xiong, D.-E. Shi, Y. Wang, B.-W. Wang, A. Ardavan, Z. Shi, S.-D. Jiang and S. Gao, *J. Am. Chem. Soc.*, 2018, **140**, 1123–1130.

11 F. Liu, G. Velkos, D. S. Krylov, L. Spree, M. Zalibera, R. Ray, N. A. Samoylova, C.-H. Chen, M. Rosenkranz, S. Schiemenz, F. Ziegs, K. Nenkov, A. Kostanyan, T. Greber, A. U. B. Wolter, M. Richter, B. Büchner, S. M. Avdoshenko and A. A. Popov, *Nat. Commun.*, 2019, **10**, 571.

12 Z. Zhu and J. Tang, *Chem. Soc. Rev.*, 2022, **51**, 9469–9481.

13 Z. Hu and S. Yang, *Chem. Soc. Rev.*, 2024, **53**, 2863–2897.

14 C. A. Gould, K. R. McClain, D. Reta, J. G. C. Kragskow, D. A. Marchiori, E. Lachman, E.-S. Choi, J. G. Analytis, R. D. Britt, N. F. Chilton, B. G. Harvey and J. R. Long, *Science*, 2022, **375**, 198–202.

15 H. Kwon, K. R. McClain, J. G. C. Kragskow, J. K. Staab, M. Ozerov, K. R. Meihaus, B. G. Harvey, E. S. Choi, N. F. Chilton and J. R. Long, *J. Am. Chem. Soc.*, 2024, **146**, 18714–18721.

16 Y.-C. Chen and M.-L. Tong, *Chem. Sci.*, 2022, **13**, 8716–8726.

17 J. Xin, Z. Hu, Y.-R. Yao, A. Ullah, X. Han, W. Xiang, H. Jin, Z. Jiang and S. Yang, *J. Am. Chem. Soc.*, 2024, **146**, 17600–17605.

18 X. Zhang, W. Li, L. Feng, X. Chen, A. Hansen, S. Grimme, S. Fortier, D. C. Sergentu, T. J. Duignan, J. Autschbach, S. Wang, Y. Wang, G. Velkos, A. A. Popov, N. Aghdassi, S. Duhm, X. Li, J. Li, L. Echegoyen, W. H. E. Schwarz and N. Chen, *Nat. Commun.*, 2018, **9**, 2753.

19 X. Zhang, Y. Wang, R. Morales-Martínez, J. Zhong, C. de Graaf, A. Rodríguez-Fortea, J. M. Poblet, L. Echegoyen, L. Feng and N. Chen, *J. Am. Chem. Soc.*, 2018, **140**, 3907–3915.

20 X. Wu and X. Lu, *J. Am. Chem. Soc.*, 2007, **129**, 2171–2177.

21 I. Infante, L. Gagliardi and G. E. Scuseria, *J. Am. Chem. Soc.*, 2008, **130**, 7459–7465.

22 C. Foroutan-Nejad, J. Vicha, R. Marek, M. Patzschke and M. Straka, *Phys. Chem. Chem. Phys.*, 2015, **17**, 24182–24192.

23 J. Zhuang, R. Morales-Martinez, J. Zhang, Y. Wang, Y. R. Yao, C. Pei, A. Rodriguez-Fortea, S. Wang, L. Echegoyen, C. de Graaf, J. M. Poblet and N. Chen, *Nat. Commun.*, 2021, **12**, 2372.

24 X. Ge, X. Dai, H. Zhou, Z. Yang and R. Zhou, *Inorg. Chem.*, 2020, **59**, 3606–3618.

25 C. F. Hermanns, M. Bernien, A. Krüger, C. Schmidt, S. T. Waßerroth, G. Ahmadi, B. W. Heinrich, M. Schneider, P. W. Brouwer, K. J. Franke, E. Weschke and W. Kuch, *Phys. Rev. Lett.*, 2013, **111**, 167203.

26 R. Westerström, A.-C. Uldry, R. Stania, J. Dreiser, C. Piamonteze, M. Muntwiler, F. Matsui, S. Rusponi, H. Brune, S. Yang, A. Popov, B. Büchner, B. Delley and T. Greber, *Phys. Rev. Lett.*, 2015, **114**, 87201.

27 T. Greber, A. P. Seitsonen, A. Hemmi, J. Dreiser, R. Stania, F. Matsui, M. Muntwiler, A. A. Popov and R. Westerström, *Phys. Rev. Mater.*, 2019, **3**, 14409.

28 Y. Feng, T. Wang, Y. Li, J. Li, J. Wu, B. Wu, L. Jiang and C. Wang, *J. Am. Chem. Soc.*, 2015, **137**, 15055–15060.

29 D. Aulakh, J. B. Pyser, X. Zhang, A. A. Yakovenko, K. R. Dunbar and M. Wriedt, *J. Am. Chem. Soc.*, 2015, **137**, 9254–9257.

30 H. Meng, C. Zhao, M. Nie, C. Wang and T. Wang, *J. Phys. Chem. C*, 2019, **123**, 6265–6269.

31 L. Hou, X. Cui, B. Guan, S. Wang, R. Li, Y. Liu, D. Zhu and J. Zheng, *Nature*, 2022, **606**, 507–510.

32 B. Peng, *J. Am. Chem. Soc.*, 2022, **144**, 19921–19931.

33 X.-K. Zhao, Y.-Y. Zhang, J. Zhao, H.-S. Hu and J. Li, *Inorg. Chem.*, 2024, **63**, 11572–11582.

34 H. Suo, M. Li, G. Yang, Y. Du, X. Zhao, X. Ren and S. Li, *Phys. Rev. B*, 2024, **110**, 125405.

35 P. Pyykkö, *J. Phys. Chem. A*, 2015, **119**, 2326–2337.

36 J. T. Boronski, J. A. Seed, D. Hunger, A. W. Woodward, J. Van Slageren, A. J. Wooles, L. S. Natrajan, N. Kaltsoyannis and S. T. Liddle, *Nature*, 2021, **598**, 72–75.

37 W. Sheng, F. Xie, T. Rajeshkumar, Y. Zhao, Y. Jiang, W. Chen, S. Ye, L. Maron and C. Zhu, *Nat. Synth.*, 2025, DOI: 10.1038/s44160-025-00789-5.

38 S. Steinberg and R. Dronskowski, *Crystals*, 2018, **8**, 225.

39 J. Zhuang, L. Abella, D. C. Sergentu, Y. R. Yao, M. Jin, W. Yang, X. Zhang, X. Li, D. Zhang, Y. Zhao, X. Li, S. Wang, L. Echegoyen, J. Autschbach and N. Chen, *J. Am. Chem. Soc.*, 2019, **141**, 20249–20260.

40 Y. Shen, X. Yu, Q. Meng, Y. R. Yao, J. Autschbach and N. Chen, *Chem. Sci.*, 2022, **13**, 12980–12986.

41 J. Burkhardt and W.-L. Li, *Inorg. Chem.*, 2024, **63**, 18313–18322.

42 Y.-L. Wang, H.-S. Hu, W.-L. Li, F. Wei and J. Li, *J. Am. Chem. Soc.*, 2016, **138**, 1126–1129.

43 B. O. Roos, P.-Å. Malmqvist and L. Gagliardi, *J. Am. Chem. Soc.*, 2006, **128**, 17000–17006.

44 F. A. Cotton, *Inorg. Chem.*, 1965, **4**, 334–336.

45 L. Gagliardi and B. O. Roos, *Nature*, 2005, **433**, 848–851.

46 X. K. Zhao, C. S. Cao, J. C. Liu, J. B. Lu, J. Li and H. S. Hu, *Chem. Sci.*, 2022, **13**, 8518–8525.

47 H.-J. Koo, D. Dai and M.-H. Whangbo, *Inorg. Chem.*, 2005, **44**, 4359–4365.

48 I. P. Muthuselvam, R. Sankar, V. N. Singh, G. N. Rao, W.-L. Lee, G.-Y. Guo and F.-C. Chou, *Inorg. Chem.*, 2015, **54**, 4303–4309.

49 S. N. Sofronova and I. I. Nazarenko, *Phys. Status Solidi B*, 2019, **256**, 1900060.